Research Article Vol. 29, No. 4 / 15 February 2021 / Optics Express 4755
Optics EXPRESS

Stress-induced deformation of the coating on large lightweight freeform optics

GUANBO QIAO,[1,2] HAIXIANG HU,[1,*] XUEJUN ZHANG,[1,2] XIAO LUO,[1] DONGLIN XUE,[1] GE ZHANG,[1] HAIFEI HU,[1] LIQI YI,[1,2] YU YANG,[1,2] AND WEIJIE DENG[1]

[1] *Changchun Institute of Optics, Fine Mechanics and Physics, Chinese Academy of Sciences, Changchun, Jilin 130033, China*
[2] *University of Chinese Academy of Sciences, Beijing 100049, China*
[*] *hhx@ciomp.ac.cn*

Abstract: Large aperture, lightweight optics are frequently utilized in modern optical systems. However, despite the use of advanced techniques for developing their materials, fabrication, and mechanical structure, the coatings placed on the substrates induce slight lattice mismatches and increase the thin film stress on polished surfaces. This significantly distorts nano-accuracy optical surfaces, especially on lightweight freeform surfaces. In this study, we construct a finite element model (FEM) and a ray tracing model to estimate the impact of the stress-induced deformation of the coating on a 1.5m class lightweight silicon carbine (SiC) mirror with a freeform surface. Our simulation results are within 10% deviation from the experimental results, and the deformation texture map matches these results as well. We discuss several possible strategies to overcome stress-induced deformation, including fabrication pre-compensation, lightweight structure redesign, and an inverse print-through effect.

1. Introduction

In recent decades, optical systems have advanced in terms of materials, fabrication, and mechanical structure [1–3]. Many large primary mirrors have achieved for high resolution and their optical surface shapes have attained nano-accuracy for high imaging quality. Furthermore, many kinds of films have been developed for different functions and wavelength bandwidths requirement. The primary mirrors are usually designed with lightweight structure to reduce the mass of the mirrors and satisfy minimal transportation requirements [4]. The lightweight ratio between the reduced mass and the solid mass for lightweight structures has reached 80% for some materials with high specific strength and stiffness, such as silicon carbide (SiC) and beryllium (Be).

Film coatings induce slight lattice mismatches between the coating and substrate materials and bring coating stress on the polished surfaces during the annealing process, which results

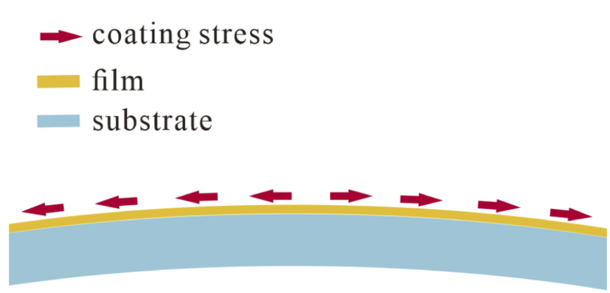

Fig. 1. Deformation caused by coating stress.

#414953 https://doi.org/10.1364/OE.414953
Journal © 2021 Received 12 Nov 2020; revised 9 Jan 2021; accepted 20 Jan 2021; published 1 Feb 2021

in bending moments on the substrates [5–13], as shown in Fig. 1. The bending stiffness of lightweight optics are smaller than those of solid optics and the films with wide wavelength are usually thick, bringing large bending moments. They lead to larger bending deformations on polished nano-accuracy surfaces. Moreover, Fig. 2 shows that the coating stress-induced deformation performs more complex on lightweight freeform optics [14,15]. This results in not only power figure errors in the surface shapes, but also special deformation textures, as shown in Figs. 2(e)–2(f), which can even damage the imaging capability of the entire system directly.

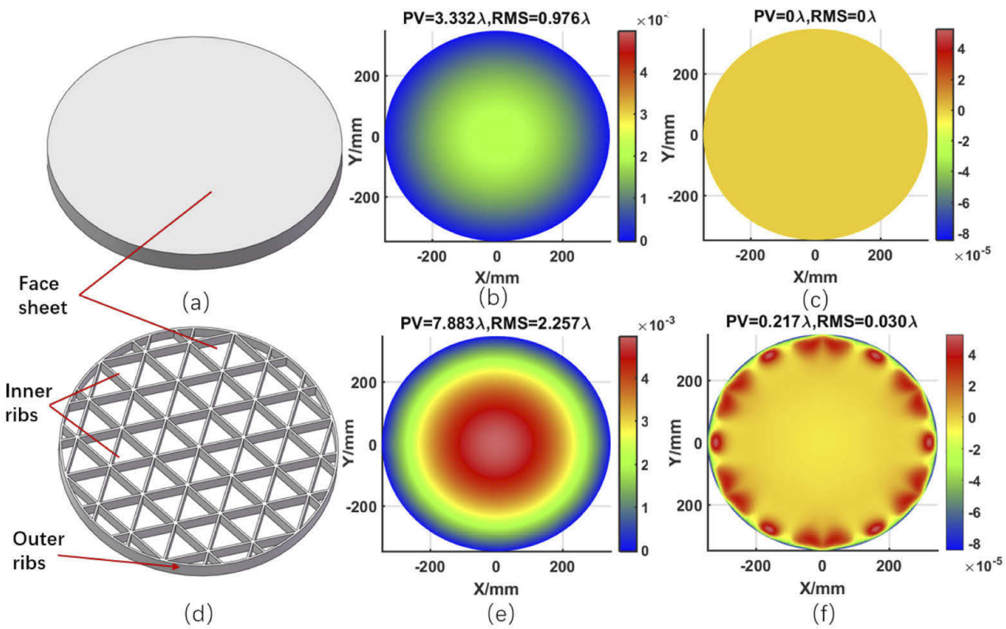

Fig. 2. (a) Solid mirror. (b) Stressed-induced deformation of coating on solid mirror. (c) Residual deformation on solid mirror without power error. (d) Lightweight mirror with triangular ribs. (e) Stressed-induced deformation of coating on lightweight mirror. (f) Residual deformation on lightweight mirror without power error.

There are two methods to prevent optical parts from coating stress-induced deformation. One is depositing the same coating on the back of the mirror as on the front [16–19]. This method is suitable for optical lens or solid mirror. But the open-structure lightweight substrates even cannot be coated on the back. Another method is to utilize ultralow stress films technologies to reduce the deformation, as reported in [20,21]. However, its application is limited, because many other kinds of film and substrate cannot be applied. Thus, is difficult to meet the requirements of wavelength bandwidth, reflectivity, manufacturing technique and equipment, etc. Also, the processing is complicated and hard to ensure safety, especially to large aperture optics. Preprocessing an inverse shape error of coating stress-induced deformation before film coating can work, provided the accurate estimation of the deformation. Preprocessing an inverse shape error of coating stress-induced deformation during surface processing can work, provided the accurate estimation of the deformation.

Coating stress, like regional thermal expansion, occurs as a lateral load, which is parallel to the surface of the optics. Stoney formula and its extensions can only be used to analyze coating stress-induced deformation on flat substrates [22–24]. Finite element method (FEM) can be used to simulate unknown physical phenomena and it has been applied to estimate the coating stress-induced deformation on flat or small aperture lightweight optics [14–15,25–26]. However, FEM has some difficulties in modeling large lightweight structures using solid elements, such as

Optics EXPRESS

poor quality of solid elements and the large number of elements to be calculated, due to the large number of small lightweight components.

In this study, we established a finite element model by shell elements and loaded bending moments successfully to simulate the stress-induced deformation of the coating on a 1.5 m class lightweight freeform reaction-bonded silicon carbide (RB-SiC) mirror. The process by which this model is formed is described in Section 2. Section 3 describes a ray tracing model of the SiC mirror with a freeform surface built to estimate the optical path error. The experimental demonstration of the coating stress-induced deformation and the method of compensating and restraining the deformation are summarized in Sections 4 and 5, respectively. The conclusion is given in Section 6.

2. Finite element modeling

Optics are usually distorted by coatings due to the lattice mismatch in the deposition process and the differential thermal expansion between the coating and substrate materials. The Stoney formula, which is the classical computational formula used to calculate the stress-induced deformation of coatings, is given by

$$\delta c = \frac{6\sigma_f t_f (1-\mu)}{E_s t_s^2} = \frac{M_f}{H}. \tag{1}$$

where δc *is* the change of curvature due to deformation, σ_f is the residual stress in the film, t_f is the film thickness, μ is the substrate Poisson ratio, E_s is the elastic modulus of the substrate, and t_s is the substrate thickness. The formula is deduced from the plates and shells theory, such that δc can be expressed as the ratio of the bending moment M_f,

$$M_f = \sigma_f t_f \frac{t_s}{2}, \tag{2}$$

to the bending stiffness *H,*

$$H = \frac{E_s t_s^3}{12(1-\mu)}. \tag{3}$$

relative to the geometrical midplane of the substrates. As the diameter and lightweight ratio of the optics increases, the bending stiffness H decreases and the stress-induced deformation of the coating increases.

The curvature deformation δc bringing a power-figure error in the surface shape results in a defocusing aberration, or power aberration, which corresponds to the fourth term in the Zernike polynomial expansion. The aberration on spherical optics can be eliminated by adjusting the position in optical system, but it introduces a new optical path error on freeform ones, which acts as a special kind of surface shape error. On lightweight mirrors, the stress-induced deformation of the coating still exists as a deformation texture without curvature deformation, which is distributed based on the position of the ribs and results in medium and high spatial frequency aberrations on the optical surface. The coating stress-induced deformation on lightweight substrates cannot be accurately described with mathematical reduction, and finite element analysis can help us to simulate numerical results.

The substrate we used was a 1.3m-long, 0.6m-wide RB-SiC freeform mirror in a shape of rectangle with rounded corners. The mirror had a semi-enclosed lightweight structure. The thickness of the back sheet is about 5 mm. The ribs are 3 mm thick, 125~190 mm high. The average thickness of the face sheet is 4.54 mm, within 0.3 mm deviation, tested by ultrasonic thickness gauge at 65 uniform distributed points. A high reflection film of 121 layers of TiO_2 and SiO_2 films were prepared by ion beam assisted electron beam evaporation. The lightweight ratio was about 86%. The areal density of the lightweight mirror was 55.07 kg/m^2. By comparison, the

Table 1. Material properties of RB-SiC mirror used in the simulations of the gravitational deformation of the optical surface.

Material	Poisson's ratio	Density	Young's modulus
RB-SiC	0.16	2980 kg/m^3	350 GPa
Aluminum	0.33	2705 kg/m^3	72 GPa
PTFE	0.4	2200 kg/m^3	280 MPa

areal density of a mirror without a lightweight structure can be much higher (up to 400 kg/m^2). The properties of the materials we used are listed in Table 1.

If 10-mm three-dimensional solid elements had been used to build the lightweight mirror's model, the number of elements would have been in the hundreds of thousands, and the quality of the elements would have been very poor. If 1.5-mm three-dimensional solid elements had been used, the number of elements would be more than 5 million, which is far beyond the elements number 200,000, that is, the ordinary computing capacity (~8G RAM). Because the thickness of the ribs and that of the surface panel were both much less than the length, high quality conventional shell elements could be used to replace solid elements and reduce the quantity by more than 2/3.

First, we simulated the change of gravitational deformation as the film is coated on the mirror surface, which is shown in Fig. 3. In the detection state, the mirror was suspended vertically and supported by four flaps made of aluminum and Teflon (polytetrafluoroethylene, PTFE). The support flaps were also included in the model.

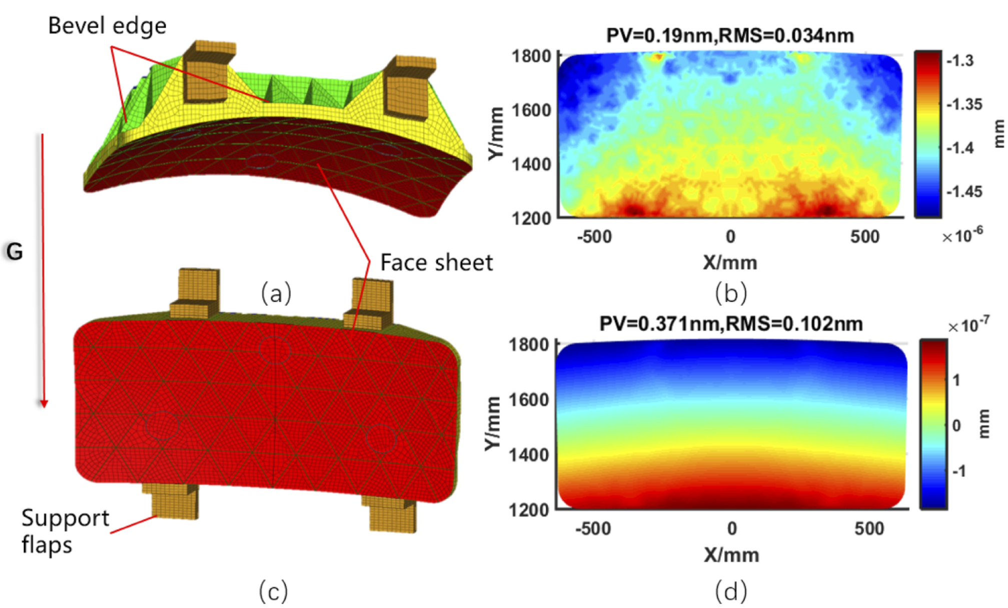

Fig. 3. (a) Finite element model in coating status. (b) The difference of gravitational deformation with and without films in coating status. (c) Finite element model in testing status. (d) The difference of gravitational deformation with and without films in testing status.

The gravitational deformation changes with the attitude of optics. Unlike the gravitational deformation, the distortion of coating stress occurs during the process of coating annealing. The stress-induced deformation of the coating depends only on temperature and properties of materials. We used 3 mm shell elements to consist the FE model and the number of elements

Optics EXPRESS

is about 200,000. The face feet had a uniform thickness 4.54 mm and the film had a uniform thickness 12.5µm. To reduce the influence of support on the coating stress-induced deformation, we added extra foam structures to provide fixed support points. In addition, we also used symmetric boundary conditions to reduce computation. We changed the temperature of the film shell to load thermal expansion and constrained the face-sheet shell and the film shell to transform the expansion to bending moment. The thin film stress was ~485 MPa, as measured the change of curvature by kSA MOS UltraScan stress indicator and calculated by Eq. (1).

Figure 4 shows the FEM result of the stress-induced deformation. The power aberration (4th term of Zernike polynomial) was about 9.05λ PV, and the residual deformation (without curvature deformation) appeared as textures on the lightweight structure. Henceforth in this paper, we refer to the residual deformation as deformation texture and the aberration caused as deformation-texture aberration.

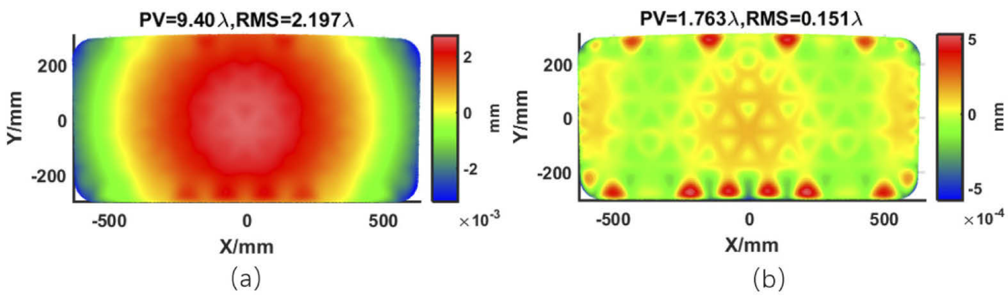

Fig. 4. (a) FEM result of the stress-induced deformation of the coating on the lightweight optics with a freeform surface. (b) Residual deformation without the 8.85λ power error.

3. Ray tracing modeling

The freeform surface of the mirror was represented by Zernike polynomials (Standard Zernike Sag in Zemax) [27]. Zernike coefficients are shown in Table 2. The radius of curvature R was 2056.63 mm and the normal radius r was 710 mm.

Table 2. Zernike [27] coefficients of the freeform surface (in mm).

Term	Value	Term	Value
a_3	4.079×10^{-1}	a_4	1.474×10^{-1}
a_6	-1.547×10^{-1}	a_7	2.0673×10^{-1}
a_9	-1.892×10^{-3}	a_{11}	7.559×10^{-2}
a_{12}	-4.952×10^{-3}	a_{14}	-3.576×10^{-5}
a_{19}	3.065×10^{-5}	a_{21}	1.140×10^{-6}
a_{22}	3.063×10^{-3}	a_{24}	-6.875×10^{-5}
a_{26}	2.260×10^{-6}	a_{29}	1.995×10^{-4}
a_{31}	-2.750×10^{-6}	a_{37}	1.017×10^{-4}

The surface shape error caused by the stress-induced deformation of the coating was mainly a power error, which resulted in a change in the radius of curvature ΔR,

$$\Delta R \approx \delta c \times R^2, \text{with } \delta c = \frac{4\delta a_4}{r^2}. \tag{4}$$

Where the peak-valley value of power figure is equal to 2 δa_4. According to Eq. (4), the radius of curvature of the surface was approximately 0.097 mm larger. A power aberration can be eliminated by translating a distance ΔR in the previous optical path, but a new aberration arises with ray propagation, as shown in Fig. 5.

$$S_1 = W_1 = \frac{cx^2 + cy^2}{1 + \sqrt{1 - c^2x^2 - c^2y^2}} + \sum a_i Z_i(x, y). \tag{5}$$

$$S_2 = \frac{kx^2 + ky^2}{1 + \sqrt{1 - k^2x^2 - k^2y^2}} + \sum a_i Z_i(x, y), \text{ with } k = c + \delta c. \tag{6}$$

$$W_2 = W_1 + \nabla W_1 \cdot \left(c^{-1} - k^{-1}\right) \approx W_1 + \nabla W_1 \cdot \frac{\delta c}{c^2}. \tag{7}$$

$$S_2 - W_2 \approx -\frac{\delta c}{c^2} \sum a_i \nabla Z_i(x, y). \tag{8}$$

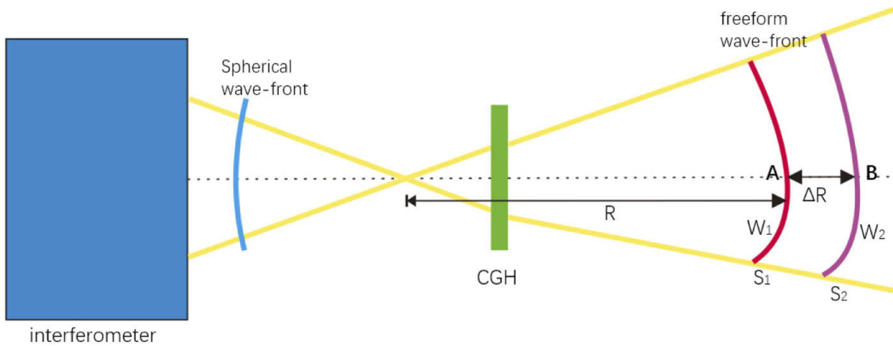

Fig. 5. Optical layout of the freeform mirror compensating test.

In Eq. (5), S_1 is the surface before coating, c is the curvature of the surface, Z_i are the Zernike terms, and a_i are the coefficients of the Zernike terms. In Eq. (6), S_2 is the surface after coating (assuming that an extra power aberration is added to the nominal surface S_1) and δc is the change in curvature. In Eq. (7), W_1 is the freeform wavefront issued at the original testing Point A by a computer-generated hologram (CGH) to test S_1, and W_2 is the new freeform wavefront after W_1 propagates a distance ΔR to Point B to match the extra power aberration. The difference between S_2 and W_2, which has no power due to the matching between S_2 and W_2, will remain in the entire

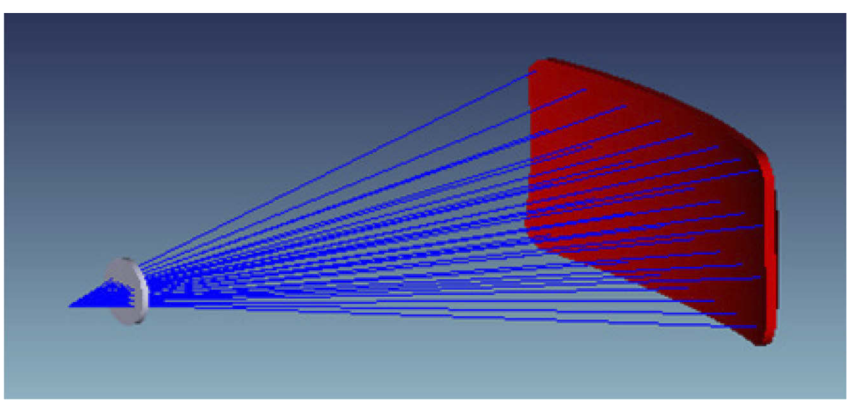

Fig. 6. Ray tracing model constructed by Zemax.

optical system as an aberration, as reduced in Eq. (8). Therefore, the whole wavefront aberration includes both deformation texture aberration and optical path aberration. A ray tracing model (in Fig. 6) is necessary to obtain the final wavefront aberration detected by the interferometer. The influence of lateral expansion is negligible (less than 0.1%).

Figure 7 shows that the translation of the mirror with a freeform surface for the purpose of eliminating the extra power aberration on the coated surface mainly caused a spherical aberration to the system with the propagation of the wavefront W_1. The result in Fig. 8 is the final simulated wavefront aberration combining the deformation texture and optical path aberrations, which can be measured by the compensating interferometry.

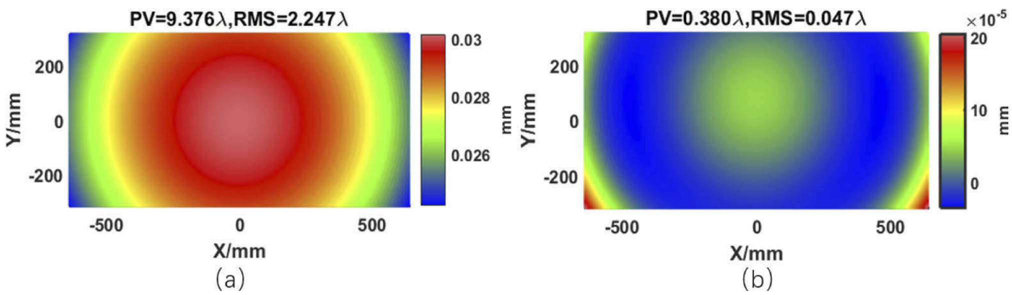

Fig. 7. (a) Difference between W_2 and W_1, i.e. ΔW. (b) Optical path difference.

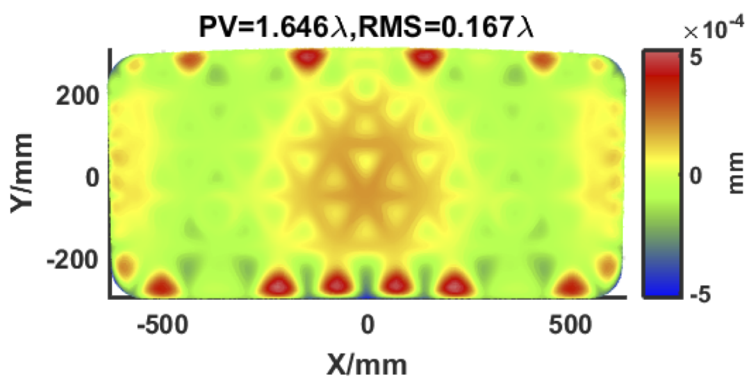

Fig. 8. Simulated test result of deform aberration, combining the deformation texture aberration and optical path difference.

4. Experimental method

4.1. Experiment setups

In order to verify the accuracy of the FEM, we coated the above-mentioned oxide film stack on a ∅150 mm, 5.37mm-thick round flat mirror as a reference. The flat mirror was tested by a Zygo interferometer, fixed by two pieces of adhesive putty, as shown in Fig. 9(a). We simulated the flat mirror in the same way, and the simulated result shows that the power aberration was -13.547λ, while the measured result shows that the power was -13.533λ. These two coating stress results are respectively tested by the kSA MOS UltraScan stress indicator and Zygo interferometer are measured on two difference mirrors with the same film coated at different times, in order to ensure the repeatability of the coating.

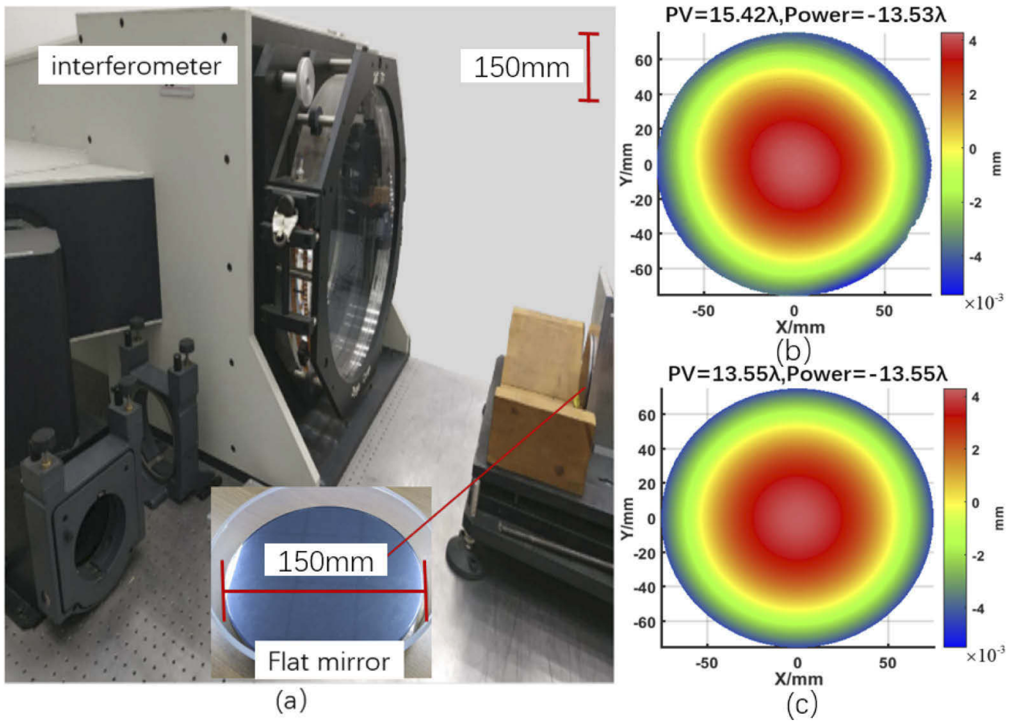

Fig. 9. (a) Flat mirror test layout. (b) Real tested deformation. (c) Simulated deformation.

We used the same equipment for evaporation coating and annealing, and the coating processes for the flat mirror and the lightweight substrate were the same.

4.2. Test results

To determine the deformation of the surface shape of the experimental mirror, we accurately measured its surface error map using a Zygo interferometer before and after the coating was applied onto the mirror, as shown in Fig. 10. The wavefront aberration could be obtained by the interferometer's charged-coupled device (CCD). The radius of curvature of this mirror was 0.10 mm larger according to the position alignment function of the CGH, within 0.01 mm test accuracy. Based on Eq. (4), the power aberration of the deformation was 9.31λ, while the FEM simulated result was 9.05λ, which corresponded to an increase in the radius of curvature by 0.097 mm. The total aberration is shown in Fig. 11. In Fig. 11(b), the colorbar was set to ±0.5μm for better comparison performance, thus some bad spots on the corner were plotted in deep blue color.

4.3. Analysis of results

The power aberrations of the simulated results and test results were similar, and the difference between the two total aberrations was less than 10%. The wavefront aberration was processed by a 1/5mm^{-1} spatial frequency, divided into low and high spatial frequency aberrations, as shown in Fig. 12. The spatial wavelength of the low spatial frequency aberration was greater than 5 mm, which corresponded to optical path difference and low-order aberrations in the wavefront error. It also reflected the variation in the low-spatial frequency bending stiffness of the lightweight optics. The high-spatial frequency error mainly corresponded to the extra bulge at the edge of the surface and the protrusions at the position of the stiffeners in the deformation texture.

Optics EXPRESS

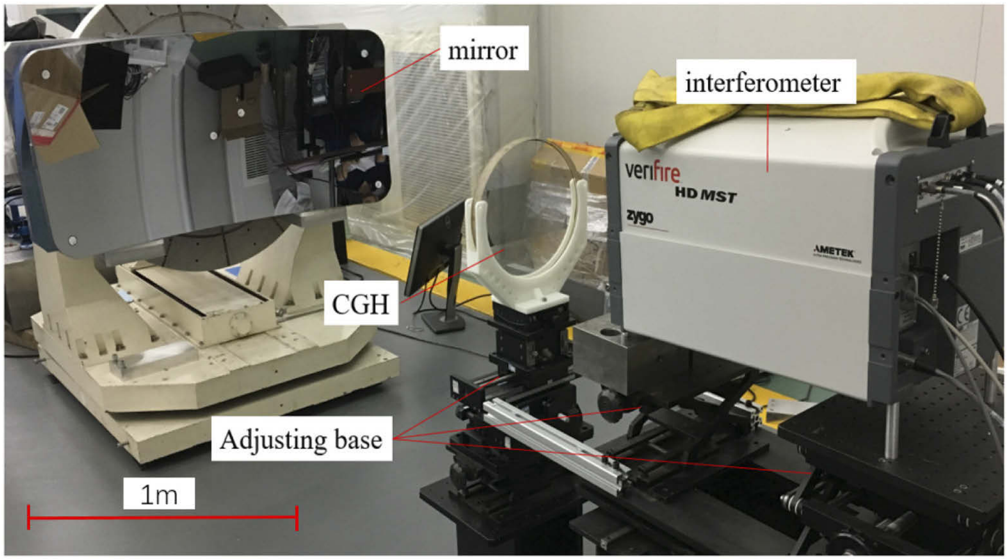

Fig. 10. Experiment layout of the freeform mirror CGH compensating test.

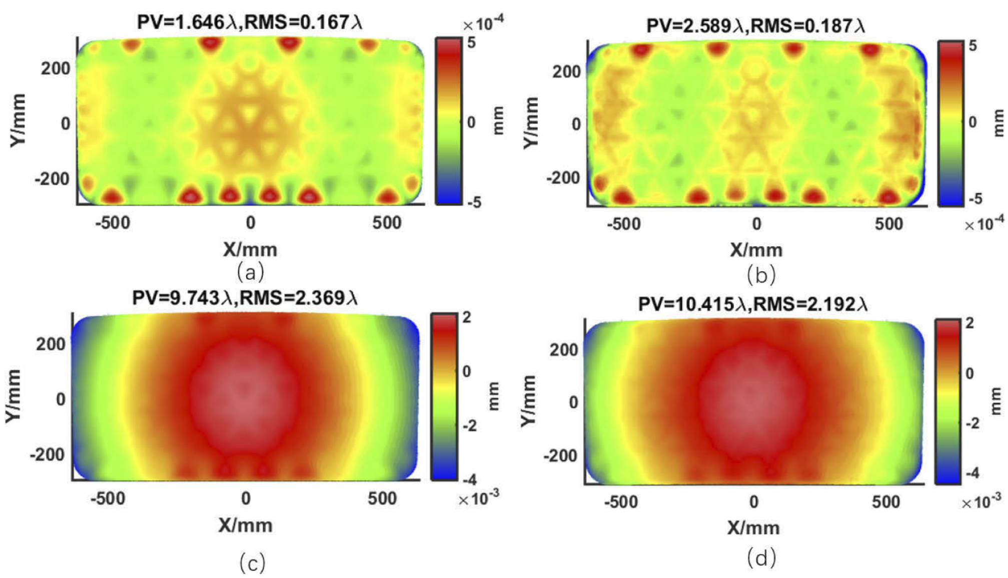

Fig. 11. (a) The simulated wavefront aberration. (b) The tested wavefront aberration. (c) The simulated deformation caused by coating stress. (d) The retrieved actual deformation, i.e. tested figure + retrieved power map according to Eq. (4).

Optics EXPRESS

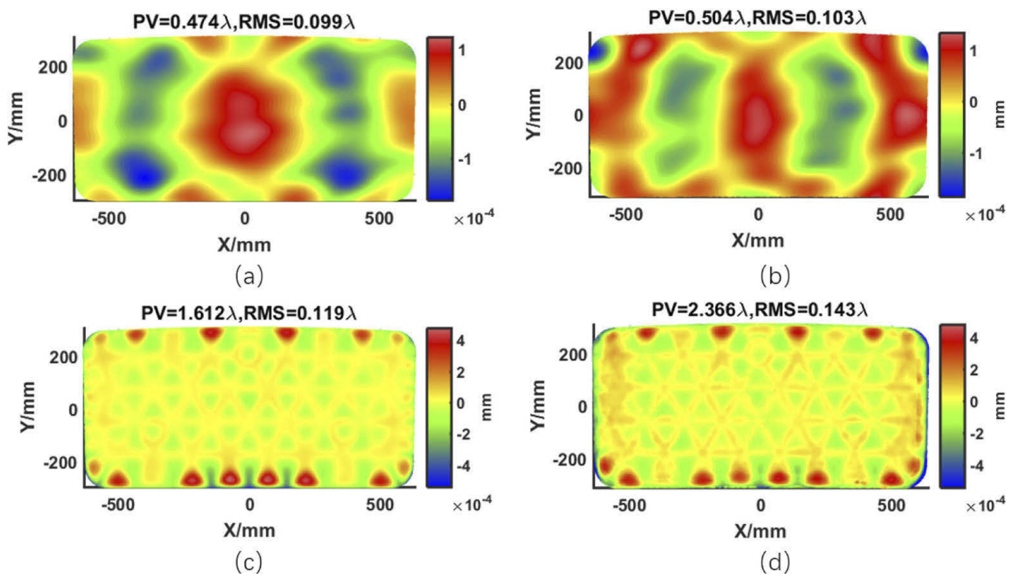

Fig. 12. (a) Low-spatial frequency error of the simulated result. (b) Low-spatial frequency error of the test result. (c) High-spatial frequency error of the simulated result. (d) High-spatial frequency error of the test result.

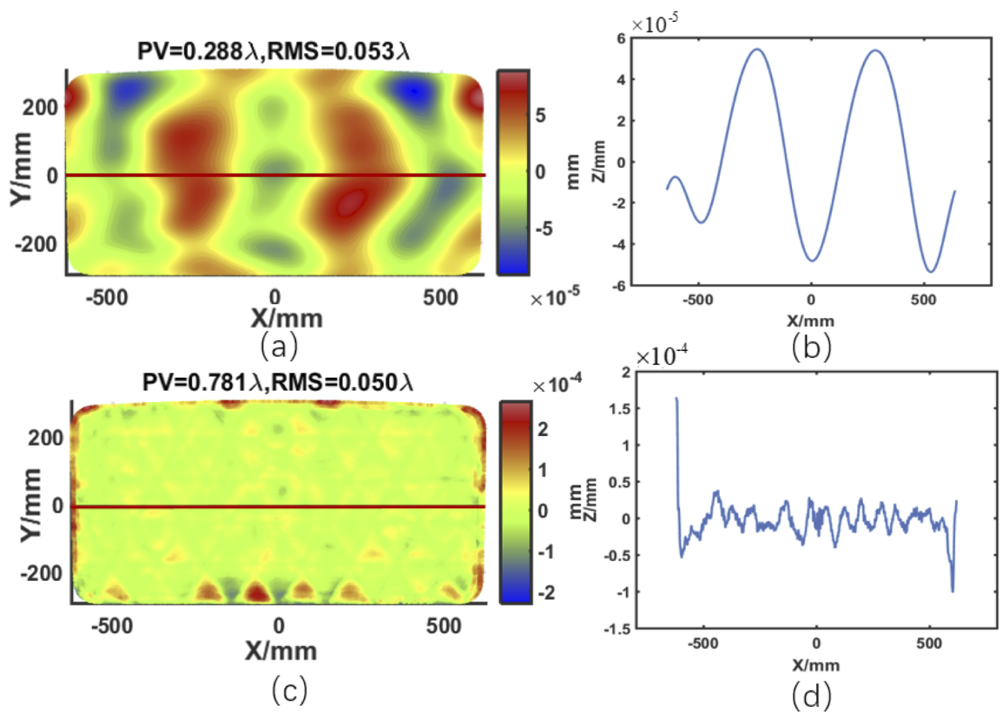

Fig. 13. (a) Difference between the two low spatial frequency aberrations. (b) Difference of low spatial frequency aberration along middle line. (c) Difference between the two high spatial frequency aberrations. (d) Difference of high spatial frequency aberration along middle line.

Optics EXPRESS

A comparison between the low-and-high-spatial frequency error of the simulation and experiment revealed slight differences between the two results, as shown in Fig. 13. There were many factors that contributed to the difference between the two low-spatial frequency error, such as the uneven thickness of the coatings, modeling parameter inaccuracy, and air turbulence in optical testing. The average thickness of inner face sheet, $-300\text{mm} \leq x \leq +300\,\text{mm}$, is about 0.2 mm thinner than the outer, which could be another factor. The coating stress bended the center region more heavily, which resulted in more spherical aberration. The main simulation error of the high spatial frequency aberration was that the deformation texture around the ribs in the test results was thinner and higher than in the simulation results. The 3 mm thick ribs were seen as a two-dimensional shell in the FEM, such that the bend deformation along the thickness could not be simulated. The regional protrusions around the ribs in the deformation texture widened and shortened this bend deformation. The rounded structure and a number of other details could not be modeled using two-dimensional shell elements, and as a result, these differences led to small errors in the simulation results. In addition, on the edge of the surface, the surface shape fluctuated significantly, inducing a regional high fringe density and leading to a large error when testing.

For the shell elements model, each element must be given a thickness, but it was impossible to assign individual thicknesses to hundreds of thousands of elements and produce a model identical to the real optics. Therefore, we needed more zoning to approximate the thickness of the actual mirror, especially the thickness of the surface panel.

5. Discussion of deformation and strategies for its mitigation

5.1. Fabrication pre-compensation

Coating is commonly the last process in optical manufacturing, and the stress-induced deformation of coatings heavily damages nano-accuracy surfaces, which perform worse on lightweight aspherical or freeform optics. For this reason, special thick films with wide wavelength bandwidths, which have large coating stresses, must be abandoned. Preprocessing an opposite aberration of the stress-induced deformation of coatings during surface processing can solve this problem. Preprocessing the surface compensated the coating stress deformation and the precision of surface improved, as shown in Fig. 14.

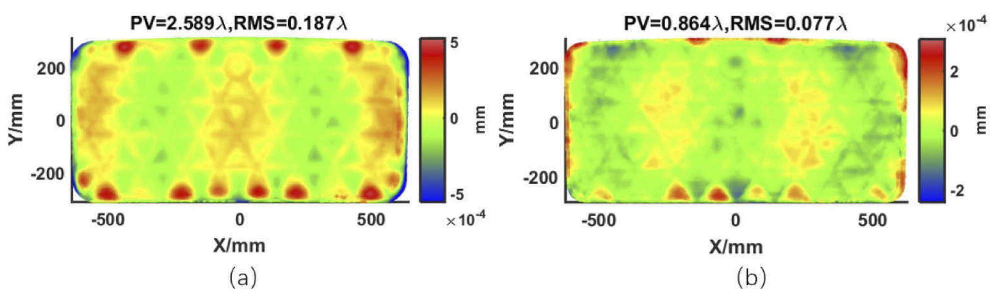

Fig. 14. (a) The tested wavefront error without compensation. (b) the difference between simulation result and test result.

The first premise of preprocessing compensation is that the simulated result is correct. The power aberration caused by the stress-induced deformation of coatings on optics with curvature could have been eliminated by adjusting the position of the optics in the imaging system, but the power error of the flat optics would have rendered the entire imaging system dysfunctional. According to the experimental results, the simulation error of the power aberration was less than 10%, and the deformation texture, the RMS of which was halved, matched this as well.

Optics EXPRESS

The second premise is that the preprocessing of the surface minimally affects the film coating and the distortion caused by the coating stress. The extra removal rate of the surface thickness was less than 0.05% for preprocessing, and the change in the stress-induced deformation of the coating was less than 0.2%, which could be ignored. The third premise is that surface preprocessing is feasible. Surface shape testing is the basis of surface accuracy processing. Although CGH design and surface testing of an opposite aberration could have been implemented, the testing figure had a slight error at the bulges and at the subsidence region of the edge of the surface due to dense regional fringes. Figure 15 shows a premium processing design for lightweight structure mirror. This method needs not only accurate estimate of the deformation, but also repeatable film stress, repeatable film thickness and uniformity of film thickness, better within a deviation of 5%.

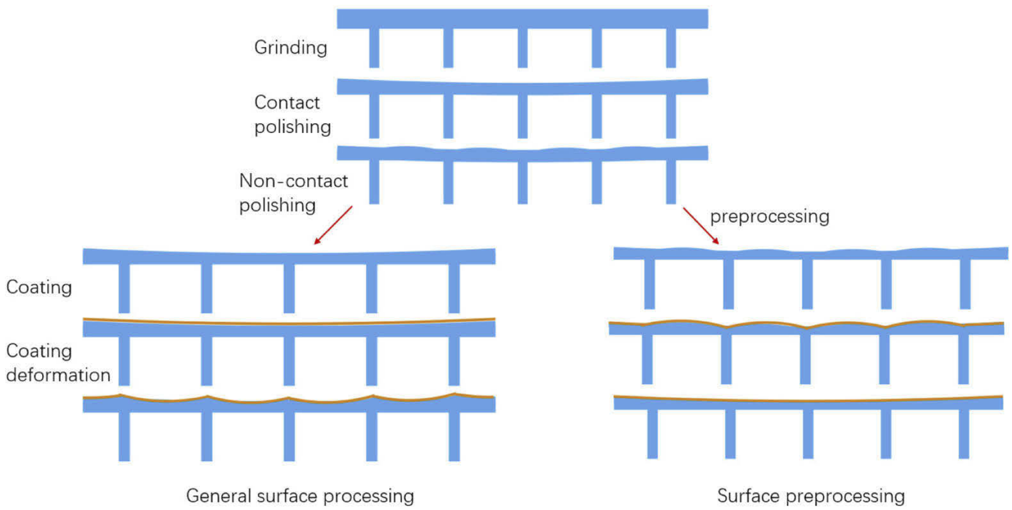

Fig. 15. Steps in surface processing and preprocessing.

5.2. Lightweight structure redesign

There were two undesirable phenomena in the deformation texture. One was bulges at the edge of the surface and the other was a type of subsidence effect on the short side and the middle of the long side of the surface. The bulges were produced by the coating stress and the bending moment caused by the outer ribs. Because of the existence of a bevel edge, the bending moment caused by the outer ribs decreased and the surface was pushed down there, which led to a subsidence phenomenon on the surface, as shown in Fig. 16. The two phenomena both induced a dense regional interference fringe during surface testing and reduced the modulation transfer function of the entire optical system. To mitigate regional flaws, the lightweight structure should be properly redesigned to minimize the effect of the two processes.

One way to restrain the bulges on the surface is to increase the stiffness of the lightweight triangle grids by thickening the surface panel or outer ribs there, which simulated result shown in Fig. 17(a). However, this method does not restrain the subsidence phenomenon. We adjusted the lightweight design by decreasing the size of the bevel edge, and the modified model balanced the coating stress and bending moment of the outer ribs. The simulation results of the modified model are shown in Fig. 17(b). The areal density of the new model changed from 55 kg/m^2 to 62 kg/m^2, and the bulges and subsidence phenomena were restrained. To maintain the nano-accuracy surface's shape and reduce the difficulty of surface testing and processing, the effect of stress-induced deformation of the coating should be considered when designing lightweight structures.

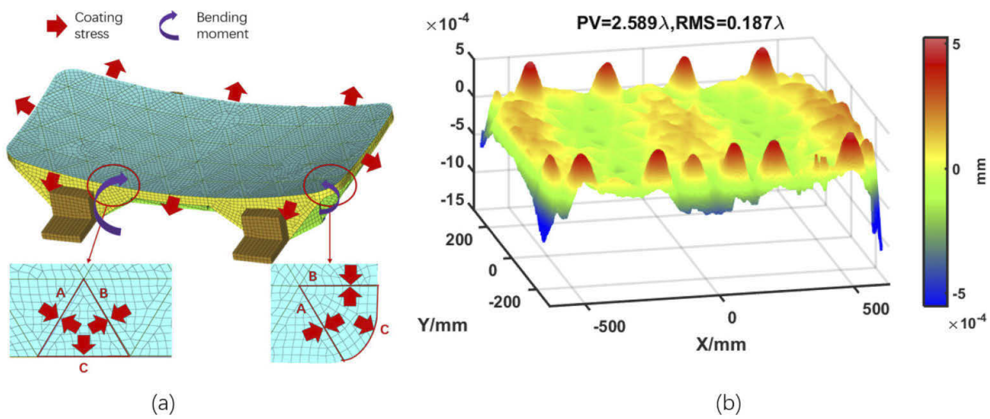

Fig. 16. (a) Expansion caused by coating stress on the lightweight mirror surface. A and B are fixed sides (where the inner ribs are) and C is a free side (where the outer rib is in the lightweight triangle grid on the fringes of the optical surface). (b) Deformation texture caused by coating stress.

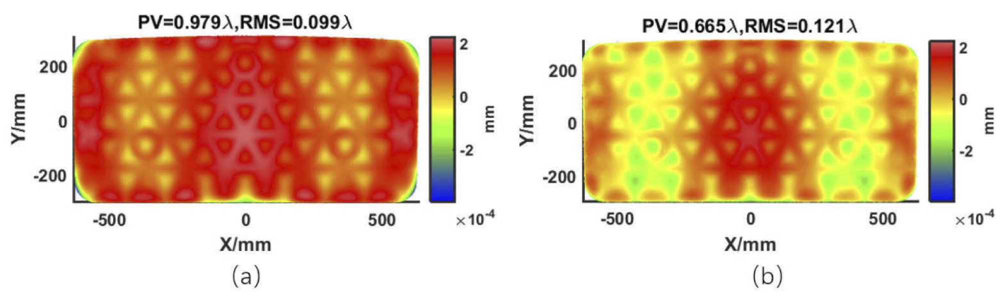

Fig. 17. (a) The simulation result of a redesigned model to restrain bulges. (b) The simulation result of a redesigned model to restrain subsidence.

5.3. Balance with print-through effect

The print-through effect is an inevitable but undesirable phenomenon in contact surface processing. The processing error caused by the print-through effect generally requires non-contact processing (such as ion-beam figuring) to remove, and it seriously affects the convergence rate of figuring [28–30]. The processing error caused by the print-through effect leads to over-polishing at the position of the ribs, as shown in Fig. 18. If the surface is uniformly removed, the surface shape error caused by the print-through effect is complementary to the high-spatial frequency error of the stress-induced deformation of the coating. Using the print-through effect to compensate for the high-spatial frequency error of the stress-induced deformation of the coating is theoretically possible. The compensation between the print-through effect and the stress-induced deformation of the coating can even reduce the workload of surface processing.

However, the roughness of the contact polished surface usually cannot reach the tolerance of the optical surface, and the magnitude of the print-through effect is related to the size of the polishing tool. We can try to develop a new process with less workload by balancing print-through effect and coating stress-induced deformation. Further research is needed to study the balance of the print-through effect and the stress-induced deformation of the coating.

Optics EXPRESS

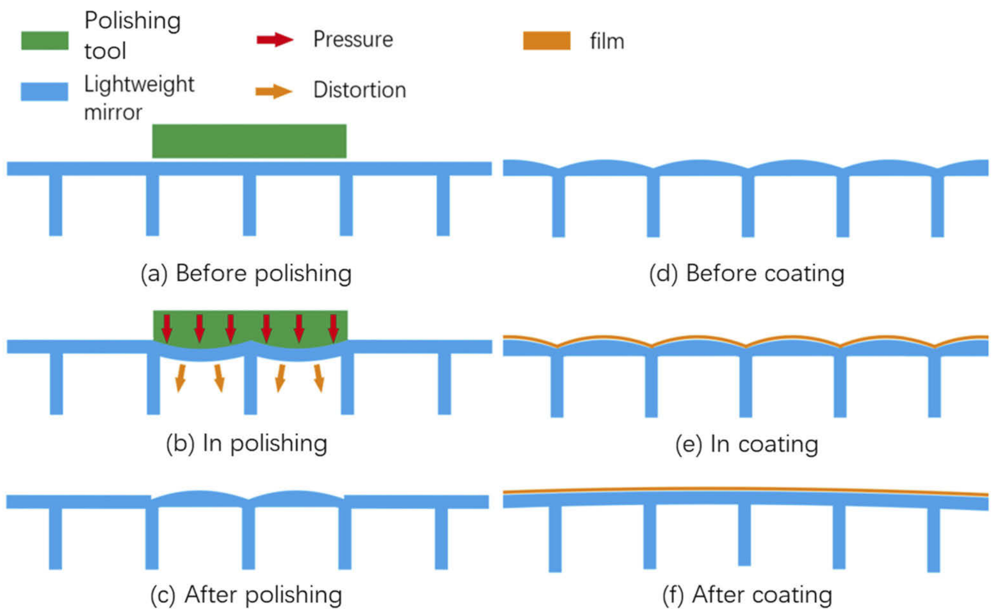

Fig. 18. (a) Before contact polishing. (b) Contact polishing tool press-in. (c) Local print-through effect caused by contact polishing. (d) Global print-through effect before coating. (e) Film stack system coating (f) Balance stress-induce deformation with the print-through effect.

6. Conclusion

Film coating stress affects the figure of optical surface, which is a large risk in high-precision surface processing, and it performs more damaging in lightweight freeform optical parts. Thus, seriously limits the decrease of area density of optics and the choose of films. We constructed a finite element model using shell elements instead solid ones to estimate this processing to reduce calculated amount and applied regional thermal field to load bending moment. We also establish a ray tracing model to obtain the optical path difference error. The simulation result of the whole wavefront error on a 1.5 m class lightweight SiC mirror was verified by the experimental interferometric test. The estimation precision was better than 10%, and the deformation texture matched well.

Based on the accurate estimation, we proposed surface preprocessing method to compensate the surface shape error caused by the coating stress-induced deformation and the difference result show that this method can improve the precision more than one time. The simulation result can also guide the design of lightweight structure to avoid regional flaws. In addition, using the print-through effect to balance the high-spatial frequency error of the coating stress-induced deformation is theoretically possible, but this requires further research, which can reduce the workload of surface processing greatly.

The estimation of the stress-induced deformation of the coating can help in choosing appropriate films to avoid the risks associated with the coating process. The compensation for the stress-induced deformation of the coating can also assist in obtaining a better surface, allowing thicker films to be applied to thin and lightweight mirrors. In addition, the estimation of the coating stress distortion should be considered when designing the lightweight structures.

Funding. Key Research Program of Frontier Sciences, CAS (QYZDJ-SSW-JSC038); Bureau of International Cooperation, Chinese Academy of Sciences (181722KYSB20180015); National Natural Science Foundation of China (11803037, 61805243); Youth Innovation Promotion Association of the Chinese Academy of Sciences (2019221).

Optics EXPRESS

Disclosures. The authors declare that there are no conflicts of interest related to this article.

References

1. M. R. Bolcar, K. Balasubramanian, J. Crooke, L. Feinberg, M. Quijada, B. J. Rauscher, D. Redding, N. Rioux, S. Shaklan, H. P. Stahl, C. M. S. tahle, and H. Thronson, "Technology gap assessment for a future large-aperture ultraviolet-optical-infrared space telescope," J. Astron. Telesc. Instrum. Syst. **2**(4), 041209 (2016).
2. M. R. Bolcar, L. D. Feinberg, K. France, B. J. Rauscher, D. Redding, and D. Schiminovich, "Initial technology assessment for the Large-Aperture UV-Optical-Infrared (LUVOIR) mission concept study," Proc. SPIE **9904**, 99040J (2016).
3. I. Trumper, P. Hallibert, J. W. Arenberg, H. Kunieda, and D. W. Kim, "Optics technology for large-aperture space telescopes: from fabrication to final acceptance tests," Adv. Opt. Photonics **10**(3), 644–702 (2018).
4. F. Wyrowski, J. T. Sheridan, Y. Meuret, P. A. Abdula, and N. D. Tolstoba, "Comparing and analysis of design lightweight large mirrors for space basing," Proc. SPIE **9889**, 98891X (2016).
5. A. E. Ennos, "Stresses Developed in Optical Film Coatings," Appl. Opt. **5**(1), 51–61 (1966).
6. W. He, M. Han, P. Goudeau, E. L. Bourhis, P. Renault, S. Wang, and L. Li, "Strain transfer through film-substrate interface and surface curvature evolution during a tensile test," Appl. Surf. Sci. **434**, 771–780 (2018).
7. Q. Lv, M. Huang, S. Zhang, S. Deng, F. Gong, F. Wang, Y. Pan, G. Li, and Y. Jin, "Effects of Annealing on Residual Stress in Ta2O5 Films Deposited by Dual Ion Beam Sputtering," Coatings **8**(4), 150 (2018).
8. S. Nakanishi, R. Kojima, and H. Kozuka, "In-plane stress development in sol–gel-derived titania and silica thin films on Si (100) substrates," J. Sol-Gel Sci. Technol. **93**(3), 506–516 (2020).
9. W. Henry, "Intrinsic stress in sputter-deposited thin films," Crit. Rev. Solid State Mater. Sci. **17**(6), 547–596 (1992).
10. L. B. Freund and S. Suresh, *Thin film materials: stress, defect formation and surface evolution* (Cambridge University Press, 2009), 750.
11. J. A. Thornton and D. W. Hoffman, "Stress-related effects in thin films," Thin Solid Films **171**(1), 5–31 (1989).
12. D. W. Hoffman and J. A. Thornton, "Internal stresses in Cr, Mo, Ta, and Pt films deposited by sputtering from a planar magnetron source," J. Vac. Sci. Technol. **20**(3), 355–358 (1982).
13. G. Thurner and R. Abermann, "Internal stress and structure of ultrahigh vacuum evaporated chromium and iron films and their dependence on substrate temperature and oxygen partial pressure during deposition," Thin Solid Films **192**(2), 277–285 (1990).
14. Y. Zhang and H. Xu, "Study on 400-1500 nm reflecting coatings on lightweight mirrors," Proc. SPIE **6721**, 67210M (2007).
15. Y. Zhang, G. Long, H. Zhou, J. Fan, H. Cui, and L. Cheng, "Finite-element-method study of the effect of thin-film residual stresses on high-order aberrations of deformable mirrors," Surf. Coat. Technol. **366**, 35–40 (2019).
16. H. Mori, T. Okajima, and W. W. Zhang, "Reflective coatings for the future x-ray mirror substrates," Proc. SPIE **10699**, 1069941 (2018).
17. Y. Yao, B. D. Chalifoux, R. K. Heilmann, and M. L. Schattenburg, "Thermal oxide patterning method for compensating coating stress in silicon substrates," Opt. Express **27**(2), 1010–1024 (2019).
18. B. D. Chalifoux, Y. Yao, and K. B. Woller, "Compensating film stress in thin silicon substrates using ion implantation," Opt. Express **27**(8), 11182–11195 (2019).
19. J. B. Oliver, J. Spaulding, and B. Charles, "Stress compensation by deposition of a nonuniform corrective coating," Appl. Opt. **59**(5), A54–57 (2020).
20. X. Lepró, P. Ehrmann, J. Menapace, J. Lotscher, S. Shin, R. Meissber, and S. Baxamusa, "Ultralow Stress, Thermally Stable Cross-Linked Polymer Films of Polydivinylbenzene (PDVB)," Langmuir **33**(21), 5204–5212 (2017).
21. D. M. Broadway, J. Weimer, and D. Gurgew, "Achieving zero stress in iridium, chromium, and nickel thin films," Proc. SPIE **9510**, 95100E (2015).
22. G. G. Stoney, "The Tension of Metallic Films Deposited by Electrolysis," Proc. R. Soc. Lond. A **82**(553), 172–175 (1909).
23. Y. Huang and A. J. Rosakis, "Extension of Stoney's formula to arbitrary temperature distributions in thin film/substrate systems," ASME," J. Appl. Mech. **74**(6), 1225–1233 (2007).
24. M. Li, J. Wu, J. He, N. Liu, T. Han, G. Zhang, and T. Yu, "An extended Stoney's formula including nonlinear deformation for large size wafer of multilayers with arbitrary thicknesses," Scr. Mater. **186**, 29–32 (2020).
25. K. A. Morse, S. L. McHugh, and J. Fixler, "Thermomechanical characterization of a membrane deformable mirror," Appl. Opt. **47**(29), 5325–5329 (2008).
26. S. Gensemer and M. Gross, "Figuring large optics at the sub-nanometer level: compensation for coating and gravity distortions," Opt. Express **23**(24), 31171–31180 (2015).
27. R. J. Noll, "Zernike polynomials and atmospheric turbulence," J. Opt. Soc. Am. **66**(3), 207–211 (1976).
28. J. Liu, X. Li, Y. Zhang, and D. Tian, "Predicting the material removal rate (MRR) in surface magnetorheological finishing (MRF) based on the synergistic effect of pressure and shear stress," Appl. Surf. Sci. **504**, 144492 (2020).
29. A. B. Shorey, W. Kordonski, and M. Tricard, "Magnetorheological finishing of large and lightweight optics," Proc. SPIE **5533**, 99–107 (2004).
30. V. Ghai, P. Ranjan, A. Batish, and H. Singh, "Atomic-level finishing of aluminum alloy by chemo-mechanical magneto-rheological finishing (CMMRF) for optical applications," J. Manuf. Proc. **32**, 635–643 (2018).